MSEC2023- 104775

CONTINUOUS FIBER PATH OPTIMIZATION IN COMPOSITE ADDITIVE MANUFACTURING VIA A FINITE ELEMENT MODEL WITH B-SPLINE FIBER PARAMETERIZATION

Molong Duan[1,2,*], Shuaiyin He[1]

[1]Hong Kong University of Science and Technology, Hong Kong SAR, China
[2]HKUST Shenzhen-Hong Kong Collaborative Innovation Research Institute, Futian, Shenzhen, China

ABSTRACT

This paper presents a finite element model of the additive manufactured part with continuous fiber reinforcement. The proposed model exploits the B-spline parameterization of the fiber path while approximating the fiber path within a triangular element to be a straight line. This simplification enables the analytical and computational-efficient calculation of the mechanical properties of the printed parts. The elements in the model are differentiated into three categories to account for the location of fiber: matrix elements, main fiber-reinforced elements, and secondary fiber-reinforced elements. Analytical formulas to calculate the geometry-dependent stiffness matrix are established. With the established finite element model with B-spline fiber parameterization, the continuous fiber path is optimized by manipulating the control points of the B-spline to reduce fiber usage while increasing the stiffness of the part. The parts with the reference and optimized carbon fiber paths are 3D printed with a continuous-fiber fused deposition method printer, with polylactic acid as the matrix material. The estimated mechanical properties of the printed parts have been verified via experimental tensile tests.

Keywords: Continuous Fiber Path Optimization, Composite Additive Manufacturing, Finite Element Model

1. INTRODUCTION

Fiber-reinforced materials, due to lightweight, high stiffness, and high strength characteristics, are widely used in air structures, automobiles, sports equipment, and wind turbine blades [1–4]. These materials are conventionally manufactured via vacuum forming, co-weaving, pultrusion, powder impregnation, and compression processes [5,6]. These manufacturing methods require complex molds with high costs, and the fibers are limited to fixed orientations. The recent development of fiber-reinforcement materials manufacturing focuses on the free manipulation of the local fiber directions and volume ratio for further using the anisotropic properties of fiber to enhance the part's mechanical properties [7]. This location-dependent manipulation of fiber is referred to as structural tailoring. The aeroelastic optimization method by finite difference [8] optimizes the local fiber direction in each spanwise wing box segment using unidirectional composite laminates. This method effectively modifies the mechanical properties by offsetting the fiber orientation, but its discontinuity causes stress concentration and potential crack formation. In comparison, fiber tow steering is an innovative solution [9] enabling continuous deposition using fiber tow prepreg [10,11]. It has the advantages of reducing stress concentrations around the geometrical discontinuous and realizing controllable mechanical properties by its variable orientation and density [12]. However, fiber tow steering has many practical manufacturing problems (e.g., delamination, wrinkle, etc.), and the high curvature fiber path is very difficult to be achieved [13]. On the other hand, additive manufacturing is another promising technology that enables structural tailoring with controllable fiber direction and distribution with a high degree of freedom [11,14].

Additive manufacturing is used to manufacture various fiber-reinforced materials, including ones with short and continuous fiber. From the different types of additive manufacturing [15], vat photopolymerization and powder bed fusion are primarily used for short fibers, while material extrusion is applicable with both short and continuous fibers. Compared to short fiber, continuous fiber can achieve significantly higher strength, stiffness, and volume ratio [16], thus contributing more to industrial applications. As the key to continuous fiber additive manufacturing, the fiber path

---

* Corresponding author: duan@ust.hk

contributes significantly to structural stiffness and strength [17], which is typically aligned with the fiber deposition direction [18].

A preliminary fiber path is commonly defined by maximizing the alignment of the fiber to the maximum stress directions [19]. However, these heuristic methods cannot guarantee the optimal distribution and orientations of the fiber path. Models of fiber paths and mechanical properties are required to perform more accurate analyses. The mechanical properties of parts with unidirectional fiber distribution have been studied. Díaz-Rodríguez et al. tested composite with different fiber volumes and compared the result with the rule of mixtures [20]. Melenka et al. used the volume average stiffness (VAS) model to predict the mechanical properties of unidirectional continuous fiber composite [21]. Abadi et al. further enhanced the VAS model with a bilinear model that can accurately predict the Poisson ratio and compared the prediction with experiment and finite element model (FEM) [22]. Mishra et al. combined the classical laminate theory with the VAS model to predict mechanical properties [23]. Polyzos et al. analyzed the fiber-reinforced composite from the fiber filament scale to the laminates scale and considered the effect of cross-section void [24]. However, these established models cannot analyze the parts with location-dependent fiber orientation and density. The load-dependent path planning (LPP) method [25] addresses this issue by converting the FEM into an optimization problem, with the direction as the optimization variable. After acquiring the desirable directions, the continuous fiber path is generated by fitting to the solution of the optimized orientation field [26,27]. However, this method does not consider the fiber location within an element, which will introduce errors in the prediction. Also, the method does not explicitly consider the fiber manufacturing and layout constraints, thus may deviate from the optimization results acquired from LPP.

This paper proposes a continuous fiber path generation and optimization method based on B-spline fiber path parameterization to fill this gap. Firstly, a FEM exploiting the B-spline parameterization of the fiber path and an open-source mesh generator by Koko [28] is established. Approximating the fiber path within a triangular element to be a straight line, the local stiffness matrix of the fiber-reinforced element is derived with similar assumptions as the VAS model. After establishing the model, the global stiffness matrix calculation workflow is designed. The fiber-reinforced elements are classified as main and secondary fiber-reinforced elements by the distance from the element vertices to the B-spline. The local stiffness matrix of each element type is calculated respectively based on the established model and assembled to the global stiffness matrix. Then, an optimization program is designed to manipulate the control points of the B-spline, aiming to increase the part stiffness and reduce fiber usage under soft geometrical constraints. Tensile tests have been performed to verify the modeling and optimization results. The FEM of the part with continuous fiber is detailed in Section 2, followed by the optimization framework detailed in Section 3. The simulation and experiment results are provided in Section 4, followed by the summary in Section 5.

2. FINITE ELEMENT MODELING OF 2-DIMENSIONAL PARTS WITH CONTINUOUS FIBER

The AM process typically involves slicing the 3-dimensional object into planar shapes to enable layer-by-layer printing. Therefore, the fiber path with conventional Cartesian 3-axis 3D printers is realized in its 2-dimensional (2D) form within a layer. Therefore, the mechanical modeling of the freeform 2D fiber path is crucial. This section established a FEM with B-Spline Fiber Parameterization (BSFP).

2.1. Finite Element Model of Straight Fiber within Triangular Mesh

Consider a three-node triangular element shown in Figure 1: the fiber within the element is assumed to be straight. This assumption is based on the fact that the mesh size is selected to be significantly smaller than the fiber's achievable radius of curvature. To reduce the model complexity and enable fiber path optimization, it is assumed that the strain within the fiber and the matrix material is the same, which is the same assumption adopted in the VAS model. It is also assumed that the contact region between the fiber boundary to the matrix is perfect without slippage (unlike the partition of unity FEM in [29]). This simplification arises from this work's focus on stiffness rather than strength.
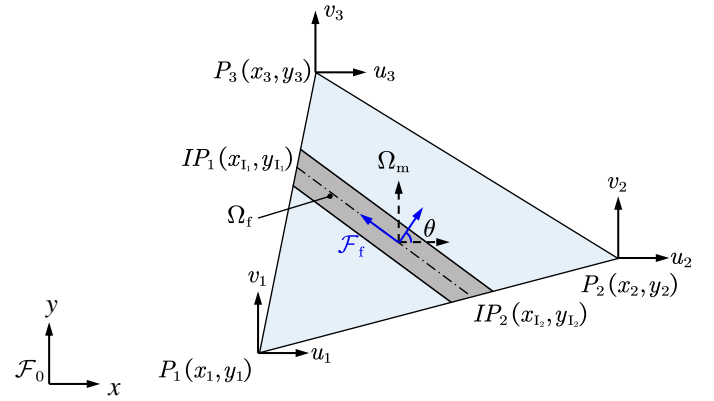

Figure 1: Three-Node Triangular Element with Fiber

Following the conventional definition of the 2D FEM formulation, the displacement field $u(x,y)$, $v(x,y)$ in one triangular element is defined as

$$\begin{cases} u(x,y) = N_1(x,y)u_1 + N_2(x,y)u_2 + N_3(x,y)u_3 \\ v(x,y) = N_1(x,y)v_1 + N_2(x,y)v_2 + N_3(x,y)v_3 \end{cases}, \quad (1)$$

where u_i and v_i $(i=1,2,3)$ are the displacements of Node P_i in the x and y axes, respectively. The shape function $N_i(x,y)$ is defined as

$$N_i = \frac{1}{2A}(a_i + b_i x + c_i y),\ i = 1,\ 2,\ 3, \quad (2)$$

where the coefficients with $N_1(x,y)$ is written as

$$A = \frac{1}{2}(a_1 + a_2 + a_3) = \frac{1}{2}(b_1 c_2 - b_2 c_1), \qquad (3)$$

$$\begin{cases} a_1 = x_2 y_3 - x_3 y_2 \\ b_1 = y_2 - y_3 \\ c_1 = -x_2 + x_3 \end{cases}. \qquad (4)$$

The coefficients with $N_2(x,y)$ and $N_3(x,y)$ are defined by alternating the subscript of Eq. (4) in a circular order (i.e., $1 \to 2, 2 \to 3, 3 \to 1$). The displacement field relationship in Eq. (1) is written in matrix form as

$$\boldsymbol{u}^{(e)}(x,y) = \begin{bmatrix} u \\ v \end{bmatrix} = \underbrace{\begin{bmatrix} N_1 & 0 & N_2 & 0 & N_3 & 0 \\ 0 & N_1 & 0 & N_2 & 0 & N_3 \end{bmatrix}}_{\boldsymbol{N}(x,y)} \boldsymbol{q}^{(e)}, \quad (5)$$

where $\boldsymbol{N}(x,y)$ is shape function matrix and $\boldsymbol{q}^{(e)}$ is the nodal degrees of freedom written as

$$\boldsymbol{q}^{(e)} = [u_1 \ v_1 \ u_2 \ v_2 \ u_3 \ v_3]^\top. \qquad (6)$$

The element strain is written as

$$\boldsymbol{\varepsilon}^{(e)}(x,y) = [\varepsilon_{xx}{}^{(e)} \ \varepsilon_{yy}{}^{(e)} \ \gamma_{xy}{}^{(e)}]^\top = [\partial]\boldsymbol{u}^{(e)}, \qquad (7)$$

where $[\partial]$ is operator matrix defined as

$$[\partial] = \begin{bmatrix} \dfrac{\partial}{\partial x} & 0 \\ 0 & \dfrac{\partial}{\partial y} \\ \dfrac{\partial}{\partial y} & \dfrac{\partial}{\partial x} \end{bmatrix}. \qquad (8)$$

Substitute Eq. (5) into Eq. (7), then the element strain is

$$\boldsymbol{\varepsilon}^{(e)}(x,y) = [\partial]\boldsymbol{N}(x,y)\boldsymbol{q}^{(e)} = \boldsymbol{B}(x,y)\boldsymbol{q}^{(e)}, \qquad (9)$$

where $\boldsymbol{B}(x,y)$ is defined as the geometry matrix.

Unlike the strain relationship that is constant within the matrix and fiber region, the stress distribution $\boldsymbol{\sigma}(x,y)$ is differentiated as

$$\boldsymbol{\sigma}(x,y) = \begin{bmatrix} \sigma_{xx}(x,y) \\ \sigma_{yy}(x,y) \\ \tau_{xy}(x,y) \end{bmatrix} = \begin{cases} \boldsymbol{D}_{\mathrm{m}}\boldsymbol{\varepsilon} & \text{when } (x,y) \in \Omega_{\mathrm{m}} \\ \boldsymbol{D}_{\mathrm{f}}\boldsymbol{\varepsilon} & \text{when } (x,y) \in \Omega_{\mathrm{f}} \end{cases}, (10)$$

where $\boldsymbol{D}_{\mathrm{m}}$ is the elastic coefficient matrix in the isotropic matrix region Ω_{m} written as

$$\boldsymbol{D}_{\mathrm{m}} = \frac{E_{\mathrm{m}}}{1-\mu^2} \begin{bmatrix} 1 & \mu & 0 \\ \mu & 1 & 0 \\ 0 & 0 & \dfrac{1-\mu}{2} \end{bmatrix}, \qquad (11)$$

and $\boldsymbol{D}_{\mathrm{f}}$ is the elastic coefficient matrix in the fiber-reinforced region Ω_{f} written as

$$\boldsymbol{D}_{\mathrm{f}} = \boldsymbol{T}(\theta)^\top \begin{bmatrix} \dfrac{E_1}{1-\mu_{12}\mu_{21}} & \dfrac{\mu_{21}E_1}{1-\mu_{12}\mu_{21}} & 0 \\ \dfrac{\mu_{21}E_1}{1-\mu_{12}\mu_{21}} & \dfrac{E_2}{1-\mu_{12}\mu_{21}} & 0 \\ 0 & 0 & G_{12} \end{bmatrix} \boldsymbol{T}(\theta). \ (12)$$

In $\boldsymbol{D}_{\mathrm{m}}$, E_{m} is matrix Young's modulus and μ is Poisson ratio; in $\boldsymbol{D}_{\mathrm{f}}$, E_1 is longitudinal Young's modulus, E_2 is transverse Young's modulus, μ_{12} and μ_{21} are in-plane Poisson ratios, G_{12} is the shear modulus; and $\boldsymbol{T}(\theta)$ is the transformation matrix from the fiber primary coordinate frame $\mathcal{F}_{\mathrm{f}}$ to the reference frame $\mathcal{F}_0$ defined as

$$\boldsymbol{T}(\theta) = \begin{bmatrix} \cos^2\theta & \sin^2\theta & 2\sin\theta\cos\theta \\ \sin^2\theta & \cos^2\theta & -2\sin\theta\cos\theta \\ -\sin\theta\cos\theta & \sin\theta\cos\theta & \cos^2\theta - \sin^2\theta \end{bmatrix}. \ (13)$$

The FEM is established via the principle of virtual work. Define the vector collection of all nodal degrees of freedom to be $\boldsymbol{q}$, the eth element's nodal displacement $\boldsymbol{q}^{(e)}$ formulates a subset of $\boldsymbol{q}$ defined with a selector matrix $\boldsymbol{T}_{\mathrm{e}}$, i.e.,

$$\boldsymbol{q}^{(e)} = \boldsymbol{T}_{\mathrm{e}}\boldsymbol{q}, \qquad (14)$$

The total potential energy Π expressed by displacement $\boldsymbol{u}$, strain $\boldsymbol{\varepsilon}$, and stress $\boldsymbol{\sigma}$ is written as

$$\begin{aligned} \Pi &= U - W_{\mathrm{b}} - W_{\mathrm{p}} - W_{\mathrm{s}} \\ &= \frac{1}{2}\int_V \boldsymbol{\varepsilon}^\top \boldsymbol{\sigma} dV - \int_V \boldsymbol{u}^\top \boldsymbol{b} dV - \boldsymbol{q}^\top \boldsymbol{p} - \int_S \boldsymbol{u}^\top \boldsymbol{t}_{\mathrm{S}} dS \\ &= \frac{1}{2}\int_V \boldsymbol{q}^\top \boldsymbol{B}^\top \boldsymbol{D}\boldsymbol{B}\boldsymbol{q}\, dV - \int_V \boldsymbol{q}^\top \boldsymbol{N}^\top \boldsymbol{b} dV - \boldsymbol{q}^\top \boldsymbol{p} \\ &\quad - \int_S \boldsymbol{q}^\top \boldsymbol{N}_{\mathrm{S}}{}^\top \boldsymbol{t}_{\mathrm{S}} dS, \end{aligned} \qquad (15)$$

where U is the strain energy; W_{b} is the potential body forces work; W_{p} is the potential concentrated loads work; W_{s} is the potential distributed loads work; V is the total volume, S is the surface where the surface traction acts; $\boldsymbol{b}$ is the body weight density matrix; $\boldsymbol{p}$ is the concentrated external loads applied at the nodes; $\boldsymbol{t}_{\mathrm{S}}$ is the surface load, and $\boldsymbol{N}_{\mathrm{S}}$ is the shape function matrix evaluated along the surface. Based on the principle of virtual work (i.e., $\delta\Pi = 0$), the FEM is written as

$$\boldsymbol{K}\boldsymbol{q} = \boldsymbol{F}, \qquad (16)$$

where both $\boldsymbol{K}$ and $\boldsymbol{F}$ is the summation from all elements, i.e.,

$$\boldsymbol{K} = \sum_{\mathrm{e}} \boldsymbol{T}_{\mathrm{e}}{}^\top \boldsymbol{K}^{(e)} \boldsymbol{T}_{\mathrm{e}}, \qquad (17)$$

$$\boldsymbol{F} = \boldsymbol{p} + \sum_{\mathrm{e}} \boldsymbol{T}_{\mathrm{e}}{}^\top \boldsymbol{F}^{(e)}. \qquad (18)$$

The local stiffness matrix $\boldsymbol{K}^{(e)}$ and local volumetric and surface force vector $\boldsymbol{F}^{(e)}$ is written as

$$\begin{aligned} \boldsymbol{K}^{(e)} &= \int_{V^{(e)}} \boldsymbol{B}^\top \boldsymbol{D}\boldsymbol{B} dV \\ &= tA_{\mathrm{f}}\boldsymbol{B}^\top \boldsymbol{D}_{\mathrm{f}}\boldsymbol{B} + tA_{\mathrm{m}}\boldsymbol{B}^\top \boldsymbol{D}_{\mathrm{m}}\boldsymbol{B}, \end{aligned} \qquad (19)$$

$$\boldsymbol{F}^{(e)} = \int_{V^{(e)}} \boldsymbol{N}^\top \boldsymbol{b} dV + \int_{S^{(e)}} \boldsymbol{N}_{\mathrm{S}}{}^\top \boldsymbol{t}_{\mathrm{S}} dS, \qquad (20)$$

where t is the element thickness, A_{f}, A_{m}, and A_{e} are areas of fiber, matrix, and the entire element; $V^{(e)}$ and $S^{(e)}$ are the element volume and surface regions where external load exists.

3. CONTINUOUS FIBER PATH OPTIMIZATION VIA B-SPLINE PARAMETERIZATION

The BSFP method aims to manipulate the fiber orientation and distribution to achieve various goals, including higher

directional stiffness, less fiber usage, etc. It parameterizes the fiber path to B-splines such that its control points formulate low-order optimization variables for convenient manipulation. The length of the B-spline is used to make the fiber usage. Then, the calculation of the element fiber area A_{f} and orientation θ is performed to obtain the part stiffness. Geometric constraints are effectively enforced via B-spline parameterization.

3.1. Preambles on the FEM Data Structure

With a defined domain Ω and its boundary $\overline{\Omega}$, the finite element is established using a triangular mesh with the node set $\boldsymbol{n} = \{n_1, n_2, \cdots, n_{n_n}\}$, element set $\boldsymbol{t} = \{t_1, t_2, \cdots, t_{n_t}\}$, and edge set $\boldsymbol{e} = \{e_1, e_2, \cdots, e_{n_e}\}$. The variables n_n, n_t, and n_e are the dimensions of $\boldsymbol{n}$, $\boldsymbol{t}$, and $\boldsymbol{e}$, respectively. The projection relationships of $\boldsymbol{n}$, $\boldsymbol{t}$, and $\boldsymbol{e}$ are defined as:

$$f_{ne}(n_i) \doteq \{e_j | n_i \text{ is a node of edge } e_j\},$$

$$f_{nt}(n_i) \doteq \{t_j | n_i \text{ is a node of element } t_j\},$$

$$f_{en}(e_i) \doteq \{n_j | e_i \text{ is an edge with node } n_j\},$$

$$f_{et}(e_i) \doteq \{t_j | e_i \text{ is an edge of element } t_j\}, \quad (21)$$

$$f_{tn}(t_i) \doteq \{n_j | t_i \text{ is an element with node } n_j\},$$

$$f_{te}(t_i) \doteq \{e_j | t_i \text{ is an element with edge } e_j\}.$$

This projection relationship is extended for element sets as input following the union operation.

3.2. Fiber Reinforced Element Classification, identification, and Calculation

B-spline is a computationally efficient way to represent freeform continuous paths and is increasingly used in additive manufacturing [30–33]. For continuous fiber with high stiffness and limited curvature, B-spline serves as a desirable parameterization of the fiber path. Assume the ith continuous fiber is parameterized with an m-degree B-spline with n_{C} control points $\boldsymbol{P}_{\mathrm{C}}^{(i)}$ defined as

$$\boldsymbol{P}_{\mathrm{C}}^{(i)} = \begin{bmatrix} x_1 & y_1 \\ x_2 & y_2 \\ \vdots & \vdots \\ x_{n_{\mathrm{C}}} & y_{n_{\mathrm{C}}} \end{bmatrix}. \quad (22)$$

The continuous fiber is thus given by a curve

$$\boldsymbol{C}^{(i)}(s) = \boldsymbol{N}^{(i)}(s)\boldsymbol{P}_{\mathrm{C}}^{(i)}, \quad (23)$$

where $\boldsymbol{N}^{(i)}(s)$ is the vector combination of the set of basis functions of the ith B-spline, and s is the curve parameter. For the convenience of computation and representation, the B-spline is densely sampled at equal spacings, i.e.,

$$\boldsymbol{C}_j^{(i)} = \boldsymbol{N}^{(i)}(s_j)\boldsymbol{P}_{\mathrm{C}}^{(i)}, \ j = 0, 1, \cdots, n_{\mathrm{s}}, \quad (24)$$

where n_{s} is the number of sampled points.

To simplify the calculation, the mesh is assumed to be sufficiently small and the fiber within an element is almost linear. Therefore, the B-spline's intersection points with the triangular mesh are linearly connected like the fiber middle line within an element. However, the finite fiber width introduced two issues:

(i) elements that contain no fiber middle line may have small portions of fiber; (ii) the fiber area within the triangular element has different shapes. To address the first issue, we explicitly define the main and secondary elements, where the main elements contain fiber middle line and the secondary elements contain fiber without the middle line, as shown in Figure 2. To address the second issue, we define four different cases:

Case 1: The fiber intersects with two edges of the triangle element without an element node inside the fiber area. The fiber area within the element is a trapezoid as shown in Figure 1. The element is the main element.

Case 2: The fiber area contains an element node whose opposite edge intersects with the fiber. The fiber area is a pentagon as shown in Element (i) in Figure 2. The element is the main element.

Case 3: The fiber area contains an element node whose two intersecting edges intersect with the fiber. The fiber area is a triangle. The element having the fiber middle line inside is the main element as shown in Element (ii) in Figure 2. The element with the fiber middle line outside is a secondary element as shown in Element (iii) in Figure 2. Two of its fiber area vertices are the average intersection points of the element edges and the fiber boundaries in the surrounding elements.

Case 4: There are two nodes inside the fiber area, i.e., an element edge is in the fiber area. The fiber area is a quadrangle. There is a pair of main (Element (iv) in Figure 2) and secondary (Element (v) in Figure 2) elements on the different sides of the edge.
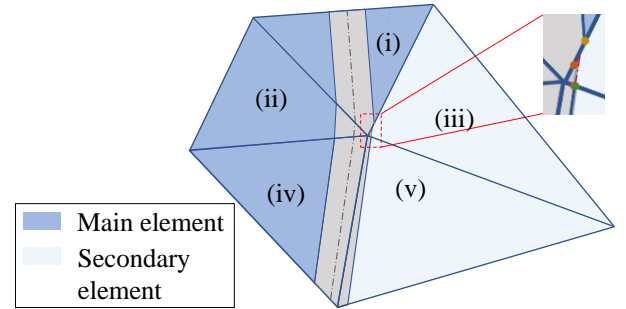

Figure 2: The Fiber Distribution Conditions Case2 (Triangle (i)), Case 3 (Triangles (ii), (iii)), and Case 4 (Triangles (iv), (v))

3.2.1. Fiber-Reinforced Elements Identification Initialization

The element containing the ith fiber's starting and ending points (i.e., $\boldsymbol{C}_0^{(i)}$ and $\boldsymbol{C}_{n_s}^{(i)}$) are first identified. The points can be either inside, on edge, or collocated with the nodes. Without loss of generality, we define $\boldsymbol{C}_0^{(i)}$ to be collocated with Node n_0, while $\boldsymbol{C}_{n_s}^{(i)}$ is inside or on the edge of an element, as shown in Figure 3. For $\boldsymbol{C}_0^{(i)}$, the potential candidates of the starting elements formulate the set

$$\{t_a, t_b, t_c, \cdots\} = f_{nt}(n_0). \quad (25)$$

The edge intersecting with the fiber further locates the reinforced element. The potential intersection edges are
$$\{e_a, e_b, e_c, \cdots\} = f_{te}(f_{nt}(n_0)) - f_{ne}(n_0). \qquad (26)$$
The intersection edge is further identified by calculating the accurate intersection point. The intersection point is on a potential edge and between the edge's nodes. Without loss of generality, two nodes of a potential Edge e_a are defined as
$$\{n_a, n_b\} = f_{en}(e_a),$$
$$n_a = \{x_a, y_a\}, \ n_b = \{x_b, y_b\}. \qquad (27)$$
The linear representation of e_a is given by
$$ax + by + c = 0, \qquad (28)$$
where
$$a = y_a - y_b,$$
$$b = x_b - x_a, \qquad (29)$$
$$c = x_a y_b - x_b y_a.$$
The accurate intersection point is defined as
$$\boldsymbol{C}^{(i)}(s_{\text{int}}) = \boldsymbol{N}^{(i)}(s_{\text{int}})\boldsymbol{P}_{\text{C}}^{(i)},$$
$$\boldsymbol{C}^{(i)}(s_{\text{int}}) = \{x_{\text{int}}, y_{\text{int}}\}. \qquad (30)$$
Use the false position method [34] to find s_{int} by calculating the root of
$$ax_{\text{int}} + by_{\text{int}} + c = 0. \qquad (31)$$
The upper and lower boundary of the false position method is marked by $\boldsymbol{C}_j^{(i)}$ and $\boldsymbol{C}_{j+1}^{(i)}$ on different sides of e_a. Specifically, the distance d_j and d_{j+1} from $\boldsymbol{C}_j^{(i)}$ and $\boldsymbol{C}_{j+1}^{(i)}$ to e_a are of different signs. The distance is given by
$$\boldsymbol{C}_j^{(i)} = \{x_j, y_j\},$$
$$d_j = (ax_j + by_j + c)/\sqrt{a^2 + b^2}. \qquad (32)$$
The intersection edge is e_a if the intersection point satisfies
$$(x_a - x_{\text{int}})(x_b - x_{\text{int}}) \leqslant 0,$$
$$(y_a - y_{\text{int}})(y_b - y_{\text{int}}) \leqslant 0. \qquad (33)$$
The starting reinforced element is t_a identified by
$$f_{nt}(n_0) \cap f_{et}(e_a) = t_a. \qquad (34)$$
Then, the location of the fiber exiting the previous element is further identified by the fiber middle line in t_a. The linear representation of the fiber middle line is given by
$$a_0 x + b_0 y + c = 0, \qquad (35)$$
where
$$\boldsymbol{C}_0^{(i)} = \{x_0, y_0\},$$
$$a_0 = y_0 - y_{\text{int}},$$
$$b_0 = x_{\text{int}} - x_0, \qquad (36)$$
$$c_0 = x_0 y_{\text{int}} - x_{\text{int}} y_0.$$
Let the fiber width be w. The fiber is identified to be originated from Node n_a of e_a if the distance from n_a to the fiber middle line is
$$d_{n_a} = (a_0 x_a + b_0 y_a + c_0)/\sqrt{a_0^2 + b_0^2} \leqslant 0.01w. \qquad (37)$$

Otherwise, the fiber exits from e_a at the intersection point. The reinforced element of the fiber ending point is identified in the same method, but the definition of potential reinforced elements is different. For the fiber ending point $\boldsymbol{C}_{n_s}^{(i)}$ shown in Element (iv) in Figure 3, Node n_{n_s} is its closest node. Intersecting Edge e_{n_s} of n_{n_s} has the smallest angle with the line formulated by n_{n_s} and $\boldsymbol{C}_{n_s}^{(i)}$. The potential reinforced elements are
$$\{t_a, t_b\} = f_{et}(e_{n_s}). \qquad (38)$$
The potential intersection edges are
$$\{e_a, e_b, e_c, \cdots\} = f_{te}(f_{et}(e_{n_s})). \qquad (39)$$
The methods to select the actual intersection edges from this set are the same as the procedure defined in Eqs. (27)~(37).
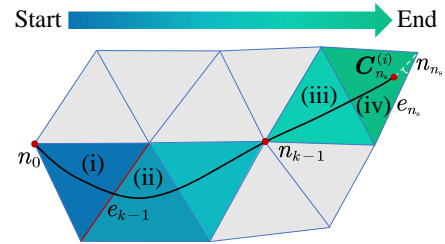

Figure 3: The illustration of Fiber Starting at a Node (i), Ending within an Element (iv), and Exiting Elements from an Edge (ii) and from a Node (iii)

3.2.2. Fiber-Reinforced Elements Consecutive Identification

The reinforced elements are consecutively identified until the ending reinforced element is reached following the initialization. This identification is achieved by the shared edge in consecutive elements. Let the previous element to be t_{k-1}, the next reinforced element and intersection edge candidates are
$$t_k = f_{et}(e_{k-1}) - t_{k-1},$$
$$\{e_a, e_b\} = f_{te}(t_k) - e_{k-1}, \qquad (40)$$
if the fiber exits from an Edge e_{k-1} as shown in Element (ii) Figure 3. However, if the fiber exits from Node n_{k-1} as shown in Element (iii) Figure 3, the potential reinforced elements and intersection edge candidates are
$$\{t_a, t_b, t_c, \cdots\} = f_{nt}(n_{k-1}) - t_{k-1},$$
$$\{e_a, e_b, e_c, \cdots\} = f_{te}(f_{nt}(n_{k-1}) - t_{k-1}) - f_{ne}(n_{k-1}). \qquad (41)$$
The accurate intersection point is calculated in the same method mentioned above to identify the reinforced element and locate the fiber exiting condition.

The methods proposed from Eqs. (25)~(41) only cover the identification of main elements. The side elements are parallelly identified by the distance from nodes to the fiber middle line. Consider main Element t_k having two intersection points $\boldsymbol{C}^{(i)}(s_{k-1})$ and $\boldsymbol{C}^{(i)}(s_k)$, the linear representation of the fiber middle line is given by
$$a_{\text{m}} x + b_{\text{m}} y + c_{\text{m}} = 0, \qquad (42)$$
where

$$\boldsymbol{C}^{(i)}(s_{k-1}) = \{x_{k-1}, y_{k-1}\},$$
$$\boldsymbol{C}^{(i)}(s_k) = \{x_k, y_k\},$$
$$a_{\mathrm{m}} = y_{k-1} - y_k, \qquad (43)$$
$$b_{\mathrm{m}} = x_k - x_{k-1},$$
$$c_{\mathrm{m}} = x_{k-1} y_k - x_k y_{k-1}.$$

Without loss of generality, the distance from Node n_a of t_k to the fiber middle line is written as

$$d_{n_a} = (a_{\mathrm{m}} x_a + b_{\mathrm{m}} y_a + c_{\mathrm{m}}) / \sqrt{a_{\mathrm{m}}^2 + b_{\mathrm{m}}^2},$$
$$\{n_a, n_b, n_c\} = f_{tn}(t_k). \qquad (44)$$

Secondary elements are identified if $d_{n_a} < w/2$; they share the common Node n_a (excluding the main elements) and are defined as

$$\boldsymbol{t}_{\mathrm{s}}^{(k)} = f_{nt}(n_a) - t_{k-1} - t_k - t_{k+1}. \qquad (45)$$

3.2.3. Fiber Orientation and Area Calculation

Consider the same Element t_k mentioned above: the fiber orientation θ is written as

$$\theta = \begin{cases} \mathrm{atan}(-a_{\mathrm{m}}/b_{\mathrm{m}}), & b_{\mathrm{m}} \neq 0 \\ \pi/2, & b_{\mathrm{m}} = 0 \end{cases}. \qquad (46)$$

The distance from the element node to the fiber middle line classifies the fiber-reinforced element cases for the calculation of the fiber area A_{f}. The calculation also applies the fiber starting and ending points by replacing the intersection points accordingly.

Case 1: The element has d_{n_a}, d_{n_b}, $d_{n_c} \geqslant w/2$ as shown in Figure 1. Its fiber area is given by

$$A_{\mathrm{f}} = \frac{1}{2} w \sqrt{(x_{k-1} - x_k)^2 + (y_{k-1} - y_k)^2}. \qquad (47)$$

Case 2: Consider the element having Node n_a inside the fiber area (i.e., $d_{n_a} < w/2$). Two edges e_b and e_c intersecting with n_a on t_k are given by

$$\{e_b, e_c\} = f_{te}(t_k) \cap f_{ne}(n_a). \qquad (48)$$

Without loss of generality, the fiber area boundary intersects at points $\boldsymbol{B}_1$ and $\boldsymbol{B}_2$ on e_b and e_c as shown in Figure 4(a). The linear representation of the fiber area boundary is given by

$$a_{\mathrm{m}} x + b_{\mathrm{m}} y + c_{\mathrm{b}} = 0,$$
$$c_{\mathrm{b}} = c_{\mathrm{m}} \pm \frac{1}{2} w [a_{\mathrm{m}} \boldsymbol{d}_{\mathrm{o}}(1) + b_{\mathrm{m}} \boldsymbol{d}_{\mathrm{o}}(2)], \qquad (49)$$

where $\boldsymbol{d}_{\mathrm{o}}$ is an offset from the fiber middle line to the fiber area boundary, given by

$$\boldsymbol{d}_{\mathrm{o}} = \left\{ \frac{1}{2} w a_{\mathrm{m}} / \sqrt{a_{\mathrm{m}}^2 + b_{\mathrm{m}}^2}, \frac{1}{2} w b_{\mathrm{m}} / \sqrt{a_{\mathrm{m}}^2 + b_{\mathrm{m}}^2} \right\}. \quad (50)$$

The fiber area is the subtraction of the trapezoid (defined in Eq. (47)) with the triangular area defined by $\triangle \boldsymbol{B}_1 \boldsymbol{B}_2 n_a$, and is given by

$$A_{\mathrm{f}} = A_{\mathrm{fo}} - \frac{\sin(\pi - \theta_a) l_1 l_2}{2},$$
$$l_1 = \sqrt{(x_{\boldsymbol{B}_1} - x_a)^2 + (y_{\boldsymbol{B}_1} - y_a)^2},$$
$$l_2 = \sqrt{(x_{\boldsymbol{B}_2} - x_a)^2 + (y_{\boldsymbol{B}_2} - y_a)^2}, \qquad (51)$$
$$\boldsymbol{B}_1 = \{x_{\boldsymbol{B}_1}, y_{\boldsymbol{B}_1}\}, \ \boldsymbol{B}_2 = \{x_{\boldsymbol{B}_2}, y_{\boldsymbol{B}_2}\},$$
$$A_{\mathrm{fo}} = \frac{1}{2} w \sqrt{(x_{k-1} - x_k)^2 + (y_{k-1} - y_k)^2},$$

where θ_a is the angle at n_a in t_k.

Case 3: Same as *Case 2*, n_a is inside the fiber area. The fiber area boundary intersects at points $\boldsymbol{B}_1$ and $\boldsymbol{B}_2$ on e_b and e_c as shown in Figure 4(b). The fiber area is given by

$$A_{\mathrm{f}} = \frac{\sin \theta_a l_1 l_2}{2},$$
$$l_1 = \sqrt{(x_{\boldsymbol{B}_1} - x_a)^2 + (y_{\boldsymbol{B}_1} - y_a)^2}, \qquad (52)$$
$$l_2 = \sqrt{(x_{\boldsymbol{B}_2} - x_a)^2 + (y_{\boldsymbol{B}_2} - y_a)^2},$$

For the secondary element, the fiber boundaries of different main elements intersect its edges in different orientations, obtaining different pairs of intersection points. The fiber area inside the secondary element is estimated by the average intersection points of the fiber boundary $\boldsymbol{B}_1^{(\mathrm{s})}$ and $\boldsymbol{B}_2^{(\mathrm{s})}$ as shown in Element (iii) Figure 2. The fiber area is given by

$$A_{\mathrm{f}} = \frac{\sin \theta_a^{(\mathrm{s})} l_1 l_2}{2},$$
$$l_1 = \sqrt{(x_{\boldsymbol{B}_1^{(\mathrm{s})}} - x_a)^2 + (y_{\boldsymbol{B}_1^{(\mathrm{s})}} - y_a)^2},$$
$$l_2 = \sqrt{(x_{\boldsymbol{B}_2^{(\mathrm{s})}} - x_a)^2 + (y_{\boldsymbol{B}_2^{(\mathrm{s})}} - y_a)^2}, \qquad (53)$$
$$\boldsymbol{B}_1^{(\mathrm{s})} = \{x_{\boldsymbol{B}_1^{(\mathrm{s})}}, y_{\boldsymbol{B}_1^{(\mathrm{s})}}\}, \ \boldsymbol{B}_2^{(\mathrm{s})} = \{x_{\boldsymbol{B}_2^{(\mathrm{s})}}, y_{\boldsymbol{B}_2^{(\mathrm{s})}}\},$$

where $\theta_a^{(\mathrm{s})}$ is the angle at n_a in the secondary element.

Case 4: Consider the element having two Nodes n_a and n_b inside the fiber area (i.e. d_{n_a}, $d_{n_b} < w/2$). An Edge e_c with n_a and n_b as nodes is given by

$$\{n_a, n_b\} = f_{en}(e_c). \qquad (54)$$

The fiber area boundary intersects at points $\boldsymbol{B}_1$ and $\boldsymbol{B}_2$ on e_b and e_c as shown in Figure 4(c). The fiber area is the subtraction of the triangular element area A_{t} with the matrix area, and is given by

$$A_{\mathrm{f}} = A_{\mathrm{t}} - \frac{1}{2} \sin \theta_c l_1 l_2,$$
$$l_1 = \sqrt{(x_{\boldsymbol{B}_1} - x_c)^2 + (y_{\boldsymbol{B}_1} - y_c)^2}, \qquad (55)$$
$$l_2 = \sqrt{(x_{\boldsymbol{B}_2} - x_c)^2 + (y_{\boldsymbol{B}_2} - y_c)^2},$$

where n_c is the node opposite to e_c, and θ_c is the angle at n_c in t_k. For the secondary element, there are also two intersection points $\boldsymbol{B}_1^{(\mathrm{s})}$ and $\boldsymbol{B}_2^{(\mathrm{s})}$. The fiber area is the addition of two triangle areas given by

$$A_f = A_{s1} + A_{s2},$$

$$A_{s1} = \frac{1}{2}\sin\theta_a^{(s)} l_1 l_2,$$

$$A_{s2} = \frac{1}{2}\sin\theta_{\boldsymbol{B}_2^{(s)}} l_3 l_4,$$

$$l_1 = \sqrt{(x_{\boldsymbol{B}_1^{(s)}} - x_a)^2 + (y_{\boldsymbol{B}_1^{(s)}} - y_a)^2},$$

$$l_2 = \sqrt{(x_b - x_a)^2 + (y_b - y_a)^2}, \tag{56}$$

$$l_3 = \sqrt{(x_{\boldsymbol{B}_1^{(s)}} - x_{\boldsymbol{B}_2^{(s)}})^2 + (y_{\boldsymbol{B}_1^{(s)}} - y_{\boldsymbol{B}_2^{(s)}})^2},$$

$$l_4 = \sqrt{(x_b - x_{\boldsymbol{B}_2^{(s)}})^2 + (y_b - y_{\boldsymbol{B}_2^{(s)}})^2},$$

where $\theta_{\boldsymbol{B}_2^{(s)}}$ is the angle between the lines $\boldsymbol{B}_2^{(s)}\boldsymbol{B}_1^{(s)}$ and $\boldsymbol{B}_2^{(s)} n_b$.
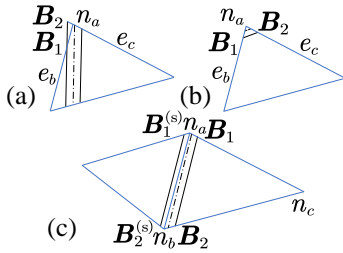
Figure 4: The Fiber Area (a) in Case 2, (b) in Case 3, and (c) in Case 4

3.3. Stiffness Evaluation and Optimization Setup

The optimization of fiber paths aims to enhance stiffness and reduce fiber usage by manipulating B-spline control points. The objective function is written as

$$f_O = \frac{L(\boldsymbol{P}_C)}{L_0} + \mu\frac{S_0}{S_p(\boldsymbol{P}_C)} + P(\boldsymbol{P}_C), \tag{57}$$

where μ is a scalar weight of the stiffness optimization, L_0 and S_0 are the characteristic values of a particular part. The length L is the fiber length written as

$$L = \sum_{i=1}^{n_f} L_B(\boldsymbol{P}_C^{(i)}), \tag{58}$$

where n_f is the number of fibers, and L_B is the length function of B-spline. The detailed part stiffness under a given displacement D is defined as

$$S_p = F_e/D. \tag{59}$$

where F_e is the calculated external force. This S_p is extracted or linearly calculated from the global stiffness matrix $\boldsymbol{K}$, follows standard finite element operations [35]. The penalty function P adds soft constraints to the optimization program, written as

$$P = E_P{}^{\boldsymbol{P}_C - \boldsymbol{P}_B}, \ \boldsymbol{P}_C > \boldsymbol{P}_B, \tag{60}$$

where E_P is the base of the penalty function, $\boldsymbol{P}_B$ is the soft boundary of control points representing the limitations of fiber distance to the boundary, inter-fiber distance, and fiber curvature.

The constraint function requires the fiber to be inside the domain written as

$$f_C = \begin{cases} -1, & \min(f_d(\boldsymbol{C}_j^{(i)})) < 0 \\ 1, & \min(f_d(\boldsymbol{C}_j^{(i)})) \geqslant 0 \end{cases}, \tag{61}$$

where $f_d(\boldsymbol{P})$ calculates the distance from a set of points $\boldsymbol{P}$ to the domain boundary.

4. SIMULATION AND EXPERIMENT RESULTS

4.1. Simulation

The program framework established in Section 3 is implemented in MATLAB with an open-source mesh generator [28] and an optimization function *fmincon*. An example part called half loop shown in Figure 5 (modified from [27]) is used for the fiber path optimization. Tensile loading applied on its top and bottom edges, the characteristic values for Eq. (57) are $L_0 = 100 \ mm$, $S_0 = 10^5 \ N/m$, and the number of control points are seven for this case.

Two optimization cases with different stiffness optimization weights μ have been simulated: a length-oriented optimization with $\mu = 0.4$ and a stiffness-oriented optimization with $\mu = 3$. The initial condition is generated from the primary stress direction (PSD), as used in [25]. The PSD and BSFP fiber paths are compared, as shown in Figure 6(a) for length-oriented optimization and Figure 6(b) for stiffness-oriented optimization. The fiber length and the part stiffness iteration process are shown in Figure 7 and Figure 8. The optimization statistics are summarized in Table 1.
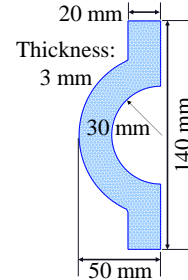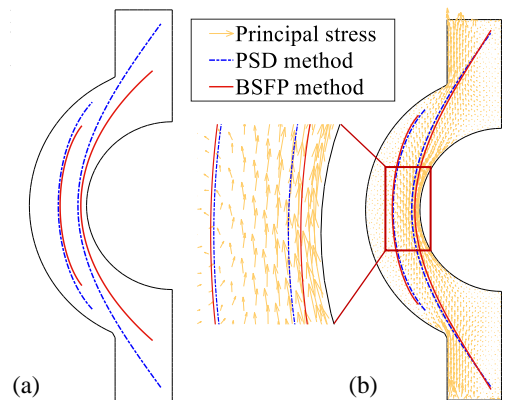

Figure 5: The Geometry of Half Loop

Figure 6: Fiber Paths Comparison of (a) Length-oriented, (b) Stiffness-oriented Optimization
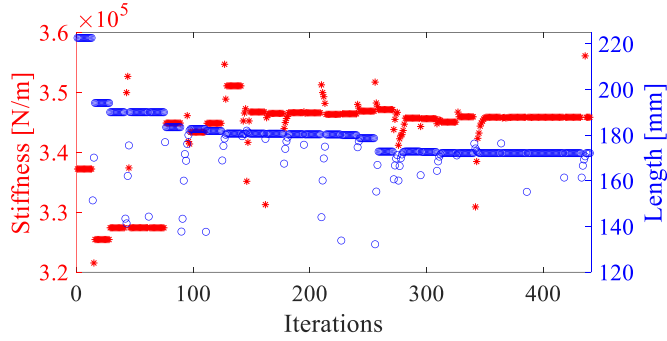
Figure 7: The Fiber Length and the Part Stiffness of Every Iteration for Length-oriented Optimization
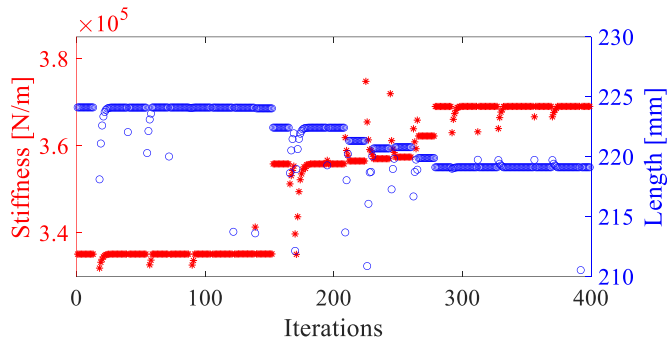

Figure 8: The Fiber Length and the Part Stiffness of Every Iteration for Stiffness-Oriented Optimization

Table 1: Comparison of the PSD Method with the BSFP Method

Case	Length-oriented	Stiffness-oriented
μ	0.4	3
Total iterations	441	401
PSD length	222.66 mm	224.11 mm
Optimized length	172.17 mm	219.12 mm
Reduction	22.68%	2.23%
PSD stiffness	335.153 N/mm	335.153 N/mm
BSFP stiffness	345.863 N/mm	369.042 N/mm
Increase	3.19%	10.11%

4.2. Experimental Verification

4.2.1. Manufacturing Platform and Parameters

The tensile test parts are fabricated by Anisoprint Composite A4 printer with a dual extruder, whose working principle and printing illustration are shown in Figure 9(a). The materials used for printing are polylactic acid (PLA) and composite carbon fiber both provided by Anisoprint SARL. Their parameters are shown in Table 2. The composite printer head co-extrudes the carbon fiber with PLA. It has a cutter 45 mm away from the nozzle to chop the fiber. As a result, the minimum fiber length must also be considered in the optimization program for actual manufacturing. The slicer software AURA enables different printing rates, layer heights, and temperatures for fiber and polymer filaments. The manufacturing parameters are selected

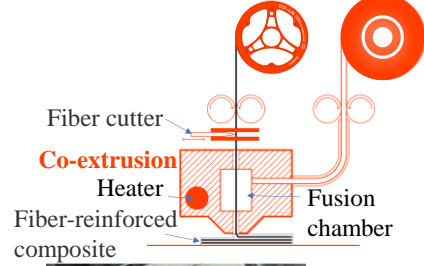based on the manufacturer's guideline [36] and are summarized in Table 3.

Figure 9: (a) Working Principle of the 3D Printer, (b) Fiber Path Detail, and (c) The MTS Sintech 10/D Fixture with the Half Loop

Table 2: The Printing Materials Parameters

Parameter	PLA	Carbon Fiber
Diameter	1.75 mm	0.35 mm
Young's modulus	3280.3 MPa	149 GPa
Tensile strength	34.7 MPa	2206 MPa
Poisson ratio	0.36	

Table 3: The 3D Printing Parameters

Temperature	215 degree C
Printing speed	40 mm/s
Layer thickness (PLA)	0.34 mm
Layer thickness (Continuous fiber)	0.17 mm
Nozzle diameter (PLA)	0.4 mm
Nozzle diameter (Continuous fiber)	0.8 mm

4.2.2. Experimental Test

The tensile tests to verify the effectiveness of the optimization program are performed on the MTS Sintech 10/D universal test machine, as shown in Figure 9(c), with a tensile speed of 2 mm/s. The PSD, intermediate, and BSFP conditions of the two cases mentioned in Section 4.1 are tested with three samples each. The resultant load-displacement curves are shown in Figure 10, with its statistics summarized in Table 4. The increase in stiffness observed experimentally is similar to that in the simulation, while the differences between the experimental results and the simulation results are also observed. For length-oriented cases, the simulation results differ from the experimental results by 10.71%, 9.69%, and 9.07% for the PSD, intermediate, and BSFP optimization stages, respectively. For stiffness-oriented cases, the differences are 10.71%, 7.77%, and 10.47%, respectively.

Based on these tensile tests, the fiber paths generated by the BSFP method are verified. However, the limitations of this study

are the low fiber volume ratio of the given part and the limited number of control points. Optimizers with higher computational efficiency are required to solve these limitations.
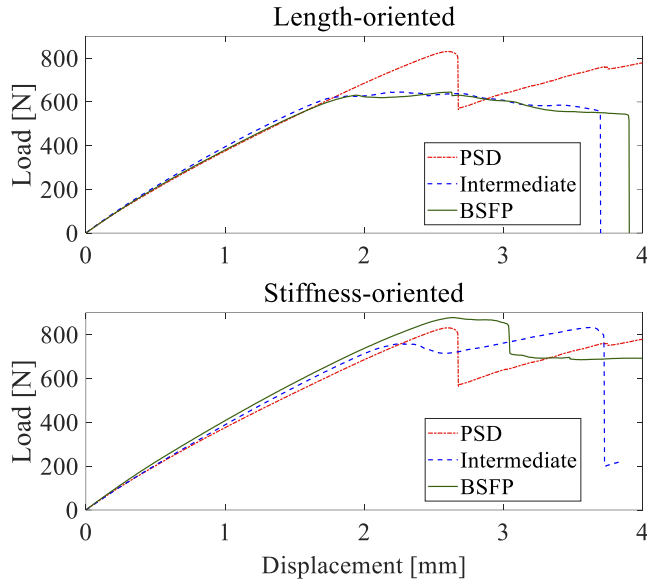

Figure 10: The Experimental Load-Displacement Comparison of PSD and BSFP Methods

Table 4: The Comparison of Part Stiffness of the PSD and BSFP Methods

Case	Length-oriented	Stiffness-oriented
PSD	375.371 N/mm	375.371 N/mm
Intermediate	383.809 N/mm	385.854 N/mm
BSFP	380.349 N/mm	412.185 N/mm
Increase	1.33%	9.81%

5. CONCLUSION

This paper established a finite element model to characterize the part reinforced by freeform continuous fiber paths. This model exploited the B-spline parameterization of the fiber paths and established the stiffness matrix calculation algorithms for the fiber-reinforced elements. This B-spline fiber parameterization converts the optimization of mechanical parts' length and stiffness to the optimization of B-spline control point locations, thus enabling computationally efficient evaluation and optimization of fiber paths. The proposed method was verified with a representative half-loop part. The part was 3D printed with fiber paths from conventional primary stress direction and the proposed method; the enhanced stiffness and fiber use reduction have been highlighted. The future work includes enhancing the fiber volume ratio, number of control points, and dedicated optimization methods.

REFERENCES

[1] Botelho, E. C., Silva, R. A., Pardini, L. C., and Rezende, M. C., 2006, "A Review on the Development and Properties of Continuous Fiber/Epoxy/Aluminum Hybrid Composites for Aircraft Structures," Mater. Res., **9**(3), pp. 247–256.

[2] Goh, G. D., Toh, W., Yap, Y. L., Ng, T. Y., and Yeong, W. Y., 2021, "Additively Manufactured Continuous Carbon Fiber-Reinforced Thermoplastic for Topology Optimized Unmanned Aerial Vehicle Structures," Compos. Part B Eng., **216**, p. 108840.

[3] Zhang, W., Tang, W. Y., Pu, Y. C., and Zhang, S. K., 2010, "Ultimate Strength Analysis of Ship Hulls of Continuous Basalt Fiber Composite Materials," Adv. Mater. Res., **150**–**151**, pp. 736–740.

[4] Bai, X., and Li, N., 2012, "The Application of Carbon Fiber Composite Material for Sports Equipment," Adv. Mater. Res., **496**, pp. 480–483.

[5] Tian, X., Liu, T., Yang, C., Wang, Q., and Li, D., 2016, "Interface and Performance of 3D Printed Continuous Carbon Fiber Reinforced PLA Composites," Compos. Part A Appl. Sci. Manuf., **88**, pp. 198–205.

[6] Wakeman, M. D., Cain, T. A., Rudd, C. D., Brooks, R., and Long, A. C., 1999, "Compression Moulding of Glass and Polypropylene Composites for Optimised Macro- and Micro-Mechanical Properties II. Glass-Mat-Reinforced Thermoplastics," Compos. Sci. Technol., **59**(5), pp. 709–726.

[7] Blok, L. G., Longana, M. L., Yu, H., and Woods, B. K. S., 2018, "An Investigation into 3D Printing of Fibre Reinforced Thermoplastic Composites," Addit. Manuf., **22**, pp. 176–186.

[8] De Leon, D. M., De Souza, C. E., Fonseca, J. S. O., and Silva, R. G. A. Da, 2012, "Aeroelastic Tailoring Using Fiber Orientation and Topology Optimization," Struct. Multidiscip. Optim., **46**(5), pp. 663–677.

[9] Rajpal, D., Mitrotta, F. M. A., Socci, C. A., Sodja, J., Kassapoglou, C., and De Breuker, R., 2021, "Design and Testing of Aeroelastically Tailored Composite Wing under Fatigue and Gust Loading Including Effect of Fatigue on Aeroelastic Performance," Compos. Struct., **275**, p. 114373.

[10] Boddeti, N., Tang, Y., Maute, K., Rosen, D. W., and Dunn, M. L., 2020, "Optimal Design and Manufacture of Variable Stiffness Laminated Continuous Fiber Reinforced Composites," Sci. Rep., **10**(1), pp. 1–15.

[11] Zhuo, P., Li, S., Ashcroft, I. A., and Jones, A. I., 2021, "Material Extrusion Additive Manufacturing of Continuous Fibre Reinforced Polymer Matrix Composites: A Review and Outlook," Compos. Part B Eng., **224**, p. 109143.

[12] Stodieck, O., Cooper, J. E., Weaver, P. M., and Kealy, P., 2013, "Improved Aeroelastic Tailoring Using Tow-Steered Composites," Compos. Struct., **106**, pp. 703–715.

[13] Sobhani Aragh, B., Borzabadi Farahani, E., Xu, B. X., Ghasemnejad, H., and Mansur, W. J., 2021, "Manufacturable Insight into Modelling and Design Considerations in Fibre-Steered Composite Laminates: State of the Art and Perspective," Comput. Methods Appl. Mech. Eng., **379**, p. 113752.

[14] Penumakala, P. K., Santo, J., and Thomas, A., 2020, "A Critical Review on the Fused Deposition Modeling of Thermoplastic Polymer Composites," Compos. Part B Eng., **201**, p. 108336.

[15] Goh, G. D., Yap, Y. L., Agarwala, S., and Yeong, W. Y., 2019, "Recent Progress in Additive Manufacturing of Fiber Reinforced Polymer Composite," Adv. Mater. Technol., **4**(1), pp. 1–22.

[16] Kabir, S. M. F., Mathur, K., and Seyam, A. M., 2020, "A Critical Review on 3D Printed Continuous Fiber-Reinforced Composites : History , Mechanism , Materials and Properties," Compos. Struct., **232**, p. 111476.

[17] Yuan, S., Li, S., Zhu, J., and Tang, Y., 2021, "Additive Manufacturing of Polymeric Composites from Material Processing to Structural Design," Compos. Part B Eng., **219**, p. 108903.

[18] Heidari-Rarani, M., Rafiee-Afarani, M., and Zahedi, A. M., 2019, "Mechanical Characterization of FDM 3D Printing of Continuous Carbon Fiber Reinforced PLA Composites," Compos. Part B Eng., **175**, p. 107147.

[19] Zhang, H., Yang, D., and Sheng, Y., 2018, "Performance-Driven 3D Printing of Continuous Curved Carbon Fibre Reinforced Polymer Composites: A Preliminary Numerical Study," Compos. Part B Eng., **151**, pp. 256–264.

[20] Díaz-Rodríguez, J. G., Pertúz-Comas, A. D., and González-Estrada, O. A., 2021, "Mechanical Properties for Long Fibre Reinforced Fused Deposition Manufactured Composites," Compos. Part B Eng., **211**, p. 108657.

[21] Melenka, G. W., Cheung, B. K. O. O., Schofield, J. S., Dawson, M. R., and Carey, J. P., 2016, "Evaluation and Prediction of the Tensile Properties of Continuous Fiber-Reinforced 3D Printed Structures," Compos. Struct., **153**, pp. 866–875.

[22] Al Abadi, H., Thai, H. T., Paton-Cole, V., and Patel, V. I., 2018, "Elastic Properties of 3D Printed Fibre-Reinforced Structures," Compos. Struct., **193**, pp. 8–18.

[23] Kumar Mishra, P., and P, S., 2020, "Prediction of In-Plane Stiffness of Multi-Material 3D Printed Laminate Parts Fabricated by FDM Process Using CLT and Its Mechanical Behaviour under Tensile Load," Mater. Today Commun., **23**.

[24] Polyzos, E., Katalagarianakis, A., Polyzos, D., Van Hemelrijck, D., and Pyl, L., 2020, "A Multi-Scale Analytical Methodology for the Prediction of Mechanical Properties of 3D-Printed Materials with Continuous Fibres," Addit. Manuf., **36**, p. 101394.

[25] Wang, T., Li, N., Link, G., Jelonnek, J., Fleischer, J., Dittus, J., and Kupzik, D., 2021, "Load-Dependent Path Planning Method for 3D Printing of Continuous Fiber Reinforced Plastics," Compos. Part A Appl. Sci. Manuf., **140**, p. 106181.

[26] Fedulov, B., Fedorenko, A., Khaziev, A., and Antonov, F., 2021, "Optimization of Parts Manufactured Using Continuous Fiber Three-Dimensional Printing Technology," Compos. Part B Eng., **227**, p. 109406.

[27] Chen, X., Fang, G., Liao, W., and Wang, C. C. L., 2022, "Field-Based Toolpath Generation for 3D Printing Continuous Fibre Reinforced Thermoplastic Composites," Addit. Manuf., **49**, p. 102470.

[28] Koko, J., 2015, "A Matlab Mesh Generator for the Two-Dimensional Finite Element Method," Appl. Math. Comput., **250**, pp. 650–664.

[29] Radtke, F. K. F., Simone, A., and Sluys, L. J., 2010, "A Partition of Unity Finite Element Method for Obtaining Elastic Properties of Continua with Embedded Thin Fibres," Int. J. Numer. Methods Eng., **84**(6), pp. 708–732.

[30] Ramani, K. S., Duan, M., Okwudire, C. E., and Ulsoy, A. G., 2017, "A Lifted Domain-Based Metric for Performance Evaluation of LTI and LTV Discrete-Time Tracking Controllers," *2017 American Control Conference*.

[31] Duan, M., Yoon, D., and Okwudire, C. E., 2018, "A Limited-Preview Filtered B-Spline Approach to Tracking Control – with Application to Vibration-Induced Error Compensation of a 3D Printer," Mechatronics, **56**, pp. 287–296.

[32] Chou, C.-H., Duan, M., and Okwudire, C. E., 2021, "A Linear Hybrid Model for Enhanced Servo Error Pre-Compensation of Feed Drives with Unmodeled Nonlinear Dynamics," CIRP Ann., **70**(1), pp. 301–304.

[33] Chou, C.-H., Duan, M., and Okwudire, C. E., 2023, "A Physics-Guided Data-Driven Feedforward Tracking Controller for Systems with Unmodeled Dynamics – Applied to 3D Printing," IEEE Access.

[34] Boman, E. C., 2009, "False Position, Double False Position and Cramer's Rule," Coll. Math. J., **40**(4), pp. 279–283.

[35] Fish, J., and Belytschko, T., 2007, *A First Course in Finite Elements*, John Wiley & Sons, Ltd.

[36] Anisoprint Sarl, "Basic Specifications" [Online]. Available: https://anisoprint.com/solutions/desktop/.